IOP Publishing Journal of Physics G: Nuclear and Particle Physics
J. Phys. G: Nucl. Part. Phys. **47** (2020) 025106 (18pp) https://doi.org/10.1088/1361-6471/ab52d3

Microscopic optical potential for ^{7}Li

Wendi Chen[1], Hairui Guo[2], Weili Sun[2], Tao Ye[2], YangJun Ying[2], Yinlu Han[3] and Qingbiao Shen[3]

[1] Graduate School of China Academy of Engineering Physics, Beijing 100088, People's Republic of China
[2] Institute of Applied Physics and Computational Mathematics, Beijing 100094, People's Republic of China
[3] Key Laboratory of Nuclear Data, China Institute of Atomic Energy, Beijing 102413, People's Republic of China

E-mail: guo_hairui@iapcm.ac.cn

Received 20 September 2019
Accepted for publication 30 October 2019
Published 9 January 2020

Abstract

A microscopic optical potential (MOP) for ^{7}Li without free parameter is obtained by folding the MOPs of its internal nucleons with their density distributions. An isospin-dependent nucleon MOP based on the Skyrme nucleon–nucleon effective interaction is used as the nucleon optical potential. Cluster model is employed to construct the internal wave function of ^{7}Li and derive the density distributions of the internal nucleons. The ^{7}Li MOP is used to calculate the elastic-scattering angular distributions and reaction cross sections for target nuclei from ^{27}Al to ^{208}Pb at incident energies up to 450 MeV. The results are compared with experimental data and the calculated results by a global phenomenological optical model potential. Generally the MOP can reproduce the experimental data reasonably well, and in many cases it is comparable to the global phenomenological optical potential.

Keywords: microscopic optical potential, ^{7}Li reaction cross section, ^{7}Li elastic scattering angular distribution

(Some figures may appear in colour only in the online journal)

1. Introduction

Optical model is one of the critical models in nuclear reaction theory, which can not only directly provide total, nonelastic, elastic scattering cross sections and elastic-scattering angular distributions, but also plays an important role in the description of inelastic scattering process, transfer reaction and compound nucleus reaction. The microscopic optical potential (MOP) differs from the phenomenological optical potential in that it need not adjust its

parameters to fit experimental data, as it is derived from nucleon–nucleon interaction theoretically. Therefore, MOP has great significance in nuclear reaction theory, particularly in the research of the nuclear reactions involving interaction systems without or lack of scattering measurement.

In recent decades, the reaction mechanism of weakly bound nuclei at energies near and below the Coulomb barrier has been a subject of great interest [1–3]. Since there is a cluster structure in weakly bound nucleus due to small separation energy, such as ^{7}Li, it may enhance the probability of breakup and transfer reactions. On the other hand, ^{7}Li induced reactions are applied in the research of the production of radioactive isotopes and nuclear astrophysics. For example, the ^{7}Li+^{nat}Zr reaction is considered to be a new route for the production of proton-rich Tc isotopes [4] which have specific clinical and biological applications. The transfer reaction ^{12}C(^{7}Li, t)^{16}O is used for indirect study of the alpha burning reaction ^{12}C(α,γ)^{16}O [5]. Therefore, optical potentials for ^{7}Li are required to understand the reaction mechanism and analyze such nuclear reactions.

A few optical potentials for ^{7}Li have been generated to analyze the experimental data so far. However, most of them can only be used for one target nucleus or at one incident energy. Zeller *et al* [6] provided a standard Woods–Saxon optical potential without spin–orbit coupling potential for ^{7}Li by fitting experimental data, which was applied to ^{208}Pb target for incident energy (EL) below 60 MeV. The phenomenological optical potential given by Sanderson *et al* [7] could be used for ^{40}Ca at EL = 34 MeV and that by Kuterbekov *et al* [8] could be applied to ^{28}Si at EL $\leqslant$ 30 MeV. Steeden *et al* [9] constructed a hybrid optical potential, whose real part was based on M3Y effective nucleon–nucleon interaction and folding model and imaginary part was a phenomenological Woods–Saxon potential, and obtained a phenomenological optical potential with Wood–Saxon form meanwhile. Both of them were suited to the incident energy at 88 MeV. Another hybrid optical potential [10], whose real part was generated by double-folding model with *G*-matrix and imaginary part was also in Woods–Saxon form, could well describe the elastic scattering angular distributions for ^{44}Ca and ^{56,58,60}Fe targets at EL = 34 MeV. Recently a new global phenomenological optical potential (GOP) for ^{7}Li was obtained by Xu *et al* [11], which was applicable to a more extensive target range.

Since the experimental data of the reaction cross section and elastic scattering angular distribution for ^{7}Li induced reactions are not abundant, the purpose of this paper is to obtain the MOP for ^{7}Li as a continuation of our series of studies on MOPs for light particles including nucleon, ^{2,3}H and ^{3,4,6}He [12–17]. This work is also aimed to investigate preliminarily the effect of the breakup coupling on the elastic channel, and make some preparations for the CDCC analysis of the breakup mechanism in ^{7}Li induced reactions based on $t + \alpha$ description of ^{7}Li and MOPs. The MOP for ^{7}Li is obtained by folding the MOPs of its constituent nucleons with their density distributions. An isospin-dependent nucleon MOP [12, 18–20] derived by using the Green's function method based on the Skyrme nucleon–nucleon interaction is applied to be the MOP of the internal nucleon of ^{7}Li. Cluster model is used to construct the internal wave function of ^{7}Li, as it presents a strong cluster structure, and to derive the density distributions of its internal nucleons. In order to evaluate the predictive power of the MOP, it is used to calculate the elastic-scattering angular distributions and reaction cross sections for targets from ^{27}Al to ^{208}Pb at incident energies up to 450 MeV.

In section 2 the formulas of the MOP for ^{7}Li are presented. Comparison and analysis of the calculated results and experimental data are given in section 3. Finally the conclusions are drawn in section 4.

2. Theoretical model

Folding model [10, 21, 22] is a powerful tool to derive optical potential for composite projectiles. In this model, the optical potential for ^{7}Li is regarded to be contributed from its internal nucleons' optical potentials and is expressed as

$$U(\vec{R}) = \int [U_n(|\vec{R} + \vec{r}|)\rho_n(\vec{r}) + U_p(|\vec{R} + \vec{r}|)\rho_p(\vec{r})]\mathrm{d}\vec{r}, \tag{1}$$

where

$$\int \rho_n(\vec{r})\mathrm{d}\vec{r} = N; \int \rho_p(\vec{r})\mathrm{d}\vec{r} = Z. \tag{2}$$

ρ_n and ρ_p are the density distributions of neutron and proton in the centre-of-mass coordinate system of the projectile, respectively. $\vec{R}$ is the relative coordinate between the center of mass of target and projectile. $\vec{r}$ is the internal coordinate of ^{7}Li. U_n and U_p are the optical potentials for neutron and proton, respectively.

U_n and U_p are isospin-dependent MOPs [12, 18–20], and here is a brief introduction. Nucleon optical potential is equivalent to the mass operator of the single-particle Green's function [23]. Thus it is possible to use nucleon–nucleon interaction with nuclear many-body theory to obtain the MOP without any free parameter. Skyrme nucleon–nucleon effective interactions were employed to derive the first- and the second-order mass operator of the single-particle Green's function through the nuclear matter approximation and the local density approximation. The first-order mass operator denoted the real part of the nucleon MOP and the imaginary part of the second-order mass operator denoted the imaginary part of the nucleon MOP [12, 20]. Good predictive power and reliability of the nucleon MOP derived from Skyrme interaction have been obtained. In this paper, the expressions of U_n and U_p are taken as those in [12, 19]. A new Skyrme interaction SKC16 [18], which can simultaneously reproduce the experimental data of the nuclear matter properties, ground-state properties and neutron-nucleus scattering well, is adopted. The incident energy of each nucleon in ^{7}Li is assumed to be one seventh of the total incident energy.

A $t + \alpha$ cluster model is adopted to describe ^{7}Li and its wave function is written as

$$\Phi_{gs} = \mathcal{A}(\varphi(\alpha)[\varphi_s(t) \otimes \chi_{l=1}(\vec{R}_r)]_{IM}), \tag{3}$$

for the ground state ($I^\pi = 3/2^-$). Here, $\mathcal{A}$ means the antisymmetrization of the nucleons. $\varphi(\alpha)$ and $\varphi_s(t)$ are the intrinsic wave functions of the alpha and tritium clusters. $\vec{R}_r$ is the relative coordinate between two clusters. χ_l represents the $t - \alpha$ relative motion with angular momentum l, which couples with the spin of tritium cluster to form the total spin I and its projection M on z axis.

In the present work, a local approximation of orthogonality condition model (OCM) [24–27] is used to calculate the relative wave function. The effects of the antisymmetrization of nucleons are taken into account approximately by employing effective intercluster potentials, $V_{\mathrm{eff}} + V_{\mathrm{eff}}^{\mathrm{so}}\vec{s} \cdot \vec{l}$, and exclude the deepest bound state as the forbidden state. The relative-motion Hamiltonian of the $t - \alpha$ system is expressed as

$$H_{t+\alpha} = T_r + V_{\mathrm{eff}} + V_{\mathrm{eff}}^{\mathrm{so}}\vec{s} \cdot \vec{l}, \tag{4}$$

where T_r represents the kinetic energies.

Since our aim is just to prepare reliable wave function of ground state ^{7}Li for deriving ρ_n and ρ_p, the effective central potential V_{eff} and effective spin–orbit potential $V_{\mathrm{eff}}^{\mathrm{so}}$ are parameterized by Gaussian form and differential Woods–Saxon form, respectively. Their detailed forms for the ground state as well as the coulomb potential V_{coul} are shown in (5)

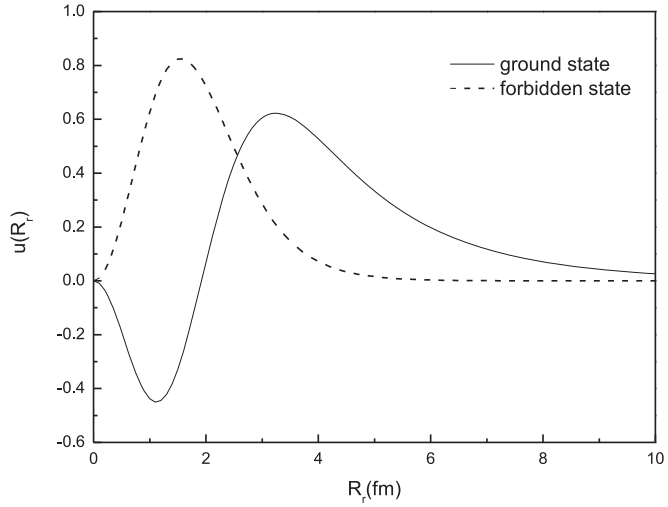

Figure 1. $u(R_r)$ ($l = 1$, $I^{\pi} = 3/2^{-}$) for the ground state and the forbidden state of ^{7}Li.

$$
\begin{aligned}
&V_{\rm eff}(R_r) = v{\rm e}^{-(R_r/a)^2} + V_{\rm coul},\\
&V^{\rm so}_{\rm eff}(R_r) = \frac{v^{\rm so}{\rm e}^{x}}{a^{\rm so}R_r(1+{\rm e}^{x})^2},\ x = (R_r - r^{\rm so})/a^{\rm so},\\
&V_{\rm coul}(R_r) = \begin{cases} Z_\alpha Z_t {\rm e}^2/R_r,\ R_r \geqslant R_{\rm cl} \\ \frac{Z_\alpha Z_t {\rm e}^2}{2R_{\rm CL}}(3 - R_r^2/R_{\rm CL}^2),\ R_r < R_{\rm cl} \end{cases}
\end{aligned}
\tag{5}
$$

where $v = -88.11$ MeV, $a = 2.447$ fm, $v^{\rm so} = -6.0$ MeV, $r^{\rm so} = 3.653\ 8$ fm, $a^{\rm so} = 0.6$ fm, $R_{\rm cl} = 1.25A_\alpha^{1/3}$ fm. A_α is the mass number of α cluster. Z_α and Z_t are the charge numbers for α and t clusters, respectively.

We calculate the $\chi_l(\vec{R}_r) = u(R_r)Y_l^m(\hat{R}_r)/R_r$ by solving the Schrodinger equation

$$(H_{t-\alpha} - E)\chi_l = 0, \tag{6}$$

and plot the $u(R_r)$ in figure 1. There are two bound-state solutions for (6) at $l = 1$ and $I^{\pi} = 3/2^{-}$, one of which with eigen-energy $E = -29.278$ MeV is eliminated as it belongs to forbidden states [27]. After excluding the forbidden state, the remaining states are orthogonal to the forbidden state, and can be regarded as the OCM wave functions. The other bound-state solution can well reproduce the energy of the ground state (-2.47 MeV from the $t - \alpha$ breakup threshold of ^{7}Li).

The spacial wave functions of t and α clusters are assumed to be $(1s)^3$ and $(1s)^4$ harmonic oscillator shell model wave functions with different oscillator constants β_t and β_α ($\beta = m\omega/\hbar$), respectively, and expressed as

$$\varphi(t) = N_t \exp\left[-\frac{\beta_t}{2}\sum_{j\in t}(\vec{r}_j - \vec{R}_t)^2\right],\ \varphi(\alpha) = N_\alpha \exp\left[-\frac{\beta_\alpha}{2}\sum_{j\in \alpha}(\vec{r}_j - \vec{R}_\alpha)^2\right], \tag{7}$$

where $\beta_t = 0.321\ 0$ fm^{-2}, $\beta_\alpha = 0.526\ 8$ fm^{-2}. $\vec{r}_j$ is the coordinate of particle j in ^{7}Li relative to the center mass of ^{7}Li. $\vec{R}_t$ and $\vec{R}_\alpha$ represent the centre of mass for the corresponding clusters. N_t and N_α are the corresponding normalized factors.

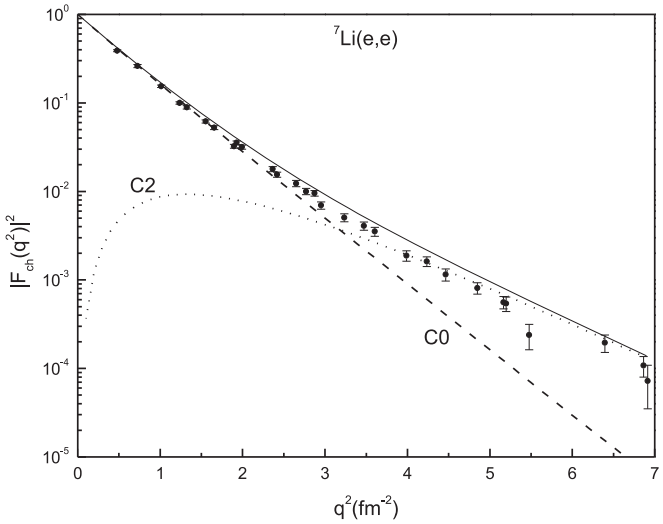

Figure 2. Charge form factors of the electron elastic scattering by ^{7}Li. The dashed and dotted lines represent the $C0$ and $C2$ contributions, respectively, and the solid line is the total result. The experimental data are taken from [28].

Charge form factors of the electron elastic scattering by ^{7}Li is then calculated by using the ground-state wave function and shown in figure 2. Since the ground state is a p state, both monopole ($C0$) and quadrupole ($C2$) contributions are taken into consideration and are shown separately. As is seen, the overall agreement between the calculated results and experimental data [28] is obtained.

The density distributions of neutron and proton, ρ_n and ρ_p, are defined as

$$\rho_{n(p)}(\vec{r}) = \langle \Phi_{gs} | \sum_{j=1}^{A} \delta(\vec{r} - \vec{r}_j) \delta_{\tau_{n(p)},\tau_j} | \Phi_{gs} \rangle, \tag{8}$$

where τ_j is the isospin of particle j. τ_n and τ_p are the isospin of neutron and proton, respectively. ρ_n and ρ_p are plotted in figure 3. The calculated value of r.m.s matter radius is 2.42 fm and that of charge radius is 2.36 fm, which reasonably agree with the experimental value [29] 2.50 $\pm$ 0.03 fm and 2.43 $\pm$ 0.03 fm, respectively.

Moreover, as the spin–orbit coupling potential contributes mainly in the surface region of the target nucleus, the nucleon spin–orbit coupling potential taken from [12, 19] should be multiplied by m^*/m, where m^* is the nucleon effective mass inside the target nucleus. Therefore the spin–orbit coupling potential for ^{7}Li is expressed as

$$V_{\rm so}(\vec{R}) = \int \mathrm{d}\vec{r} \left[\frac{m_n^*}{m_n} V_{{\rm so},n}(|\vec{R} + \vec{r}|)\rho_n(\vec{r}) + \frac{m_p^*}{m_p} V_{{\rm so},p}(|\vec{R} + \vec{r}|)\rho_p(\vec{r}) \right], \tag{9}$$

where $V_{{\rm so},n}$ and $V_{{\rm so},p}$ are the spin–orbit coupling potentials for neutron and proton, respectively.

3. Calculated result and analysis

The MOP of ^{7}Li obtained in section 2 is analyzed and used to calculate the elastic-scattering angular distributions and reaction cross sections for target nuclei from ^{27}Al to ^{208}Pb.

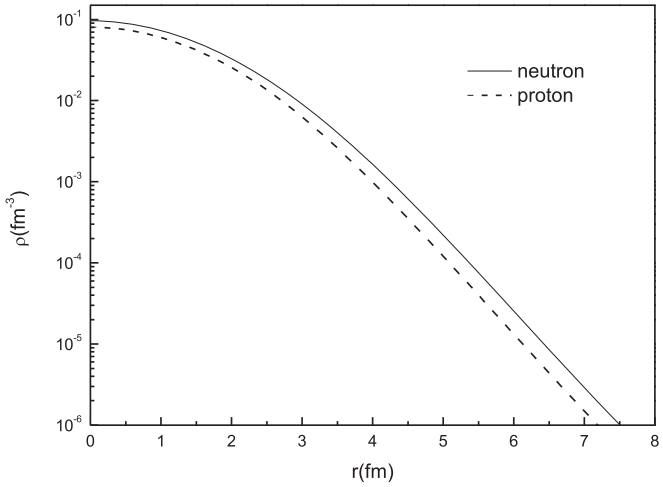

Figure 3. Density distributions of neutron (ρ_n) and proton (ρ_p) of ^{7}Li.

The radial dependence of the MOP for ^{7}Li+^{208}Pb reaction at incident energies 10 MeV, 100 MeV and 300 MeV is shown in figure 4. With the increase of incident energy and radius, the absolute value of the real part (V) decreases. However the depth of the imaginary part (W) increases somewhat at first and then decreases as radius increases and the contribution of W changes from the dominant surface absorption to the volume absorption with the increasing incident energy.

The calculated elastic-scattering angular distributions in the Rutherford ratio at EL = 34 MeV are compared with experimental data [7, 10, 30] and those calculated by the GOP taken from [11] as shown in figure 5. In the following figures, experimental data and the calculated results by the MOP and the GOP are always plotted together to be compared. A good performance on reproducing the measured elastic-scattering angular distributions for ^{56}Fe, ^{60,62}Ni, ^{64,68}Zn and ^{90}Zr targets is observed for MOP. However the calculated results are larger than the experimental data for ^{40,44,48}Ca, especially for ^{40}Ca, when the scattering angle is larger than 60°. For the GOP calculation, a good agreement with experimental data has been obtained for most of targets but it underestimates the experimental data for ^{40}Ca above 90°.

The elastic-scattering angular distributions at EL = 17 MeV for ^{46,48}Ti targets are presented in figure 6. The results obtained from the MOP are in a good agreement with the experimental data [31].

Similar comparisons are made at EL = 52 MeV for ^{140}Ce and ^{142}Nd targets in figure 7. A good agreement with the experimental data [32, 33] is obtained for the MOP.

The calculated elastic-scattering angular distributions for ^{28}Si target are compared with experimental data [34–36] at incident energies from 8.0 MeV to 36.0 MeV in figure 8. A good agreement is observed when EL $\leqslant$ 26.0 MeV and the scattering angle is less than 70°, whereas an underestimation occurs above 70°. The situation is similar for the GOP. In addition, the calculated results are in reasonable agreement with experimental data at incident energy 36 MeV except for angles above 60°.

In figure 9, the calculated elastic-scattering angular distributions for ^{80}Se at incident energies from 14.0 MeV to 26.0 MeV are shown. The calculated results from the MOP are in good agreement with experimental data [37] in most cases and match them better than the

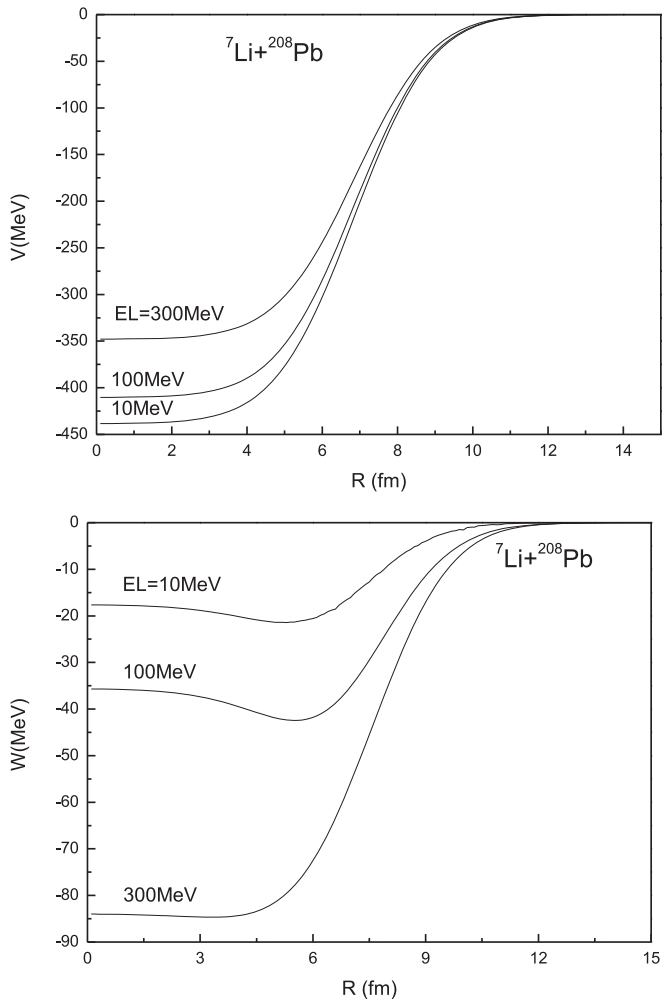

Figure 4. Radial dependence of the real part (V) and the imaginary part (W) of the MOP for ^{7}Li+^{208}Pb reaction.

GOP results at EL = 19.0 and 20.0 MeV. At the incident energy 18.0 MeV, theoretical results from both MOP and GOP are smaller than the experimental data above 110°.

The calculated elastic-scattering angular distributions for ^{120}Sn targets are shown in figure 10. Generally, a good agreement with experimental data [38–40] is obtained for the MOP, expect some slight underestimation for back angles at relatively high incident energies. The MOP results reproduce the experimental data better than the GOP results do for large angles at EL $\leqslant$ 22MeV, but worse above 22 MeV.

The elastic-scattering angular distributions for ^{144}Sm are presented in figure 11. Similarly as ^{120}Sn, the MOP reproduces the experimental data [33, 41] generally well and slightly underestimates the measured data for large angles at higher incident energies.

In figure 12, the calculated elastic-scattering angular distributions for ^{208}Pb are compared with experimental data [6, 42–44] from 27.0 MeV to 52.0 MeV. Results from the MOP are in good agreement with experimental data except for the case at EL = 33.0 MeV, where the results are slightly smaller than the measured data at the large angles. In addition, the MOP

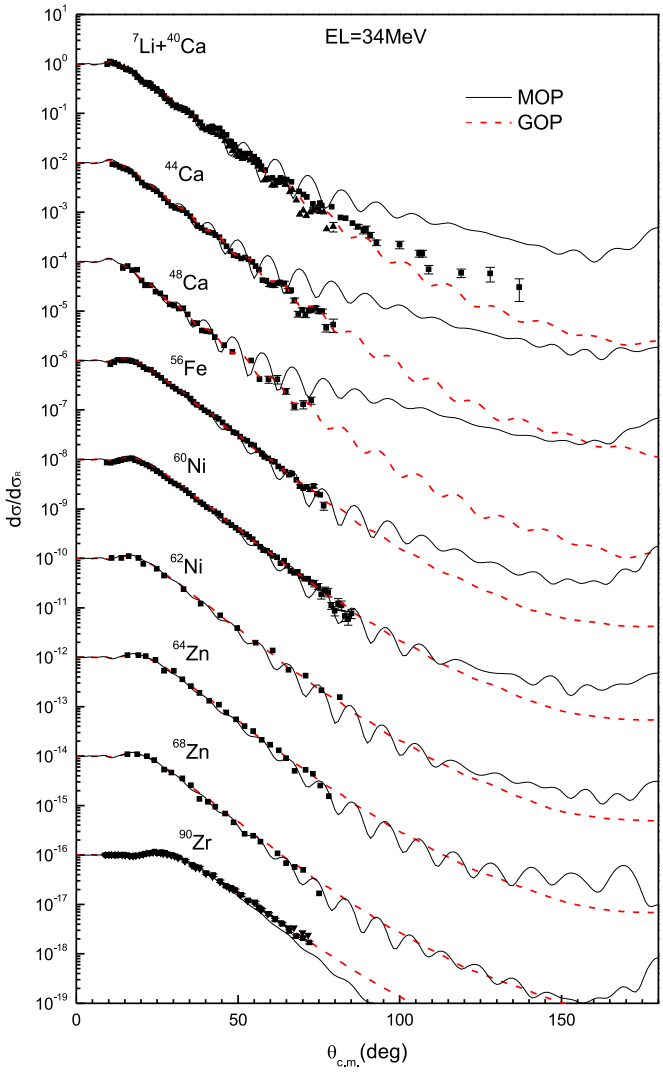

Figure 5. Calculated elastic-scattering angular distributions in the Rutherford ratio at incident energy 34.0 MeV compared with experimental data [7, 10, 30]. The solid lines and dashed lines denote the results calculated by the MOP and the GOP [11], respectively.

results reproduce the experimental data better than the GOP results do at incident energies of 39 MeV and 52 MeV.

In some experiments, the elastic-scattering angular distributions are measured for specific scattering angles at different incident energies. Figure 13 shows the comparison between the calculated results and experimental data [45–47] for ^{28}Si and ^{48}Ti targets at scattering angles 140° and 170°. Theoretical results calculated by the MOP and the GOP are both in reasonable agreement with the experimental data.

Besides the elastic-scattering angular distribution, we calculate the reaction cross sections of ^{7}Li induced reactions on ^{12}C, ^{27}Al, ^{28}Si, ^{64}Zn, ^{nat}Cu, ^{116}Sn, ^{138}Ba, ^{208}Pb, and compare

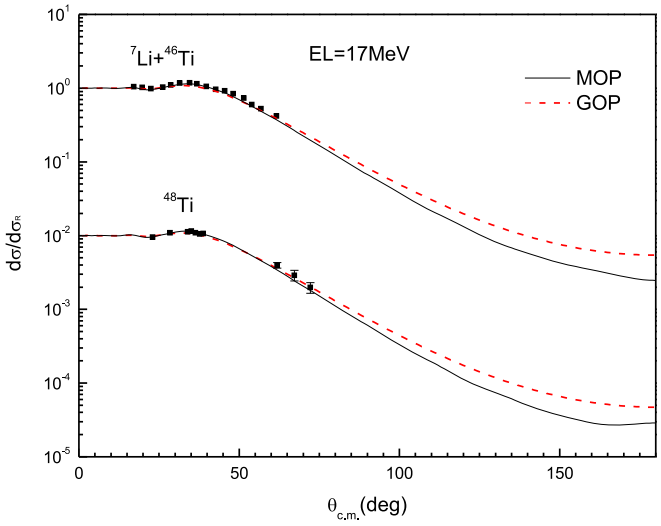

Figure 6. Same as figure 5 but at EL = 17.0 MeV. The experimental data are taken from [31].

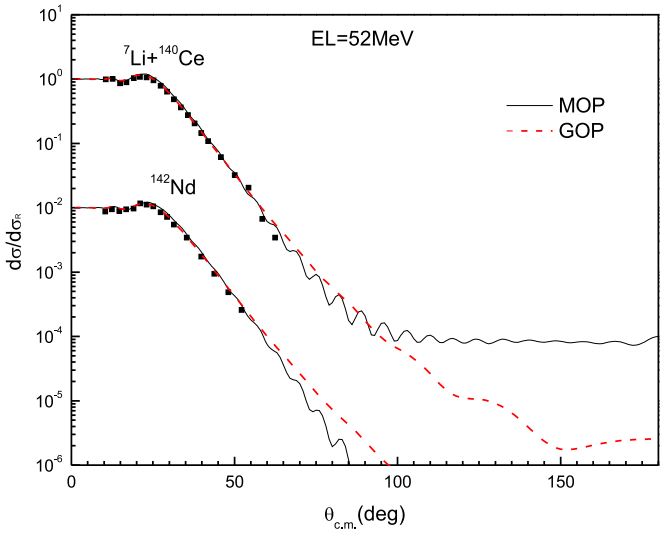

Figure 7. Same as figure 5 but at EL = 52.0 MeV. The experimental data are taken from [32, 33].

them with experimental data and the values calculated by the GOP. Among the targets, the reaction cross section for ^{nat}Cu is calculated by averaging the reaction cross sections for ^{65}Cu and ^{63}Cu over their natural abundance.

Figure 14 presents the calculated reaction cross sections and experimental data for ^{13}C [48], ^{28}Si [49–53], ^{nat}Cu [54] and ^{208}Pb [41, 43]. For ^{12}C, it can be seen that the theoretical value is within the error range. The calculated results for ^{28}Si by the MOP are in good agreement with experimental data below 30 MeV but they give a slight overestimation at

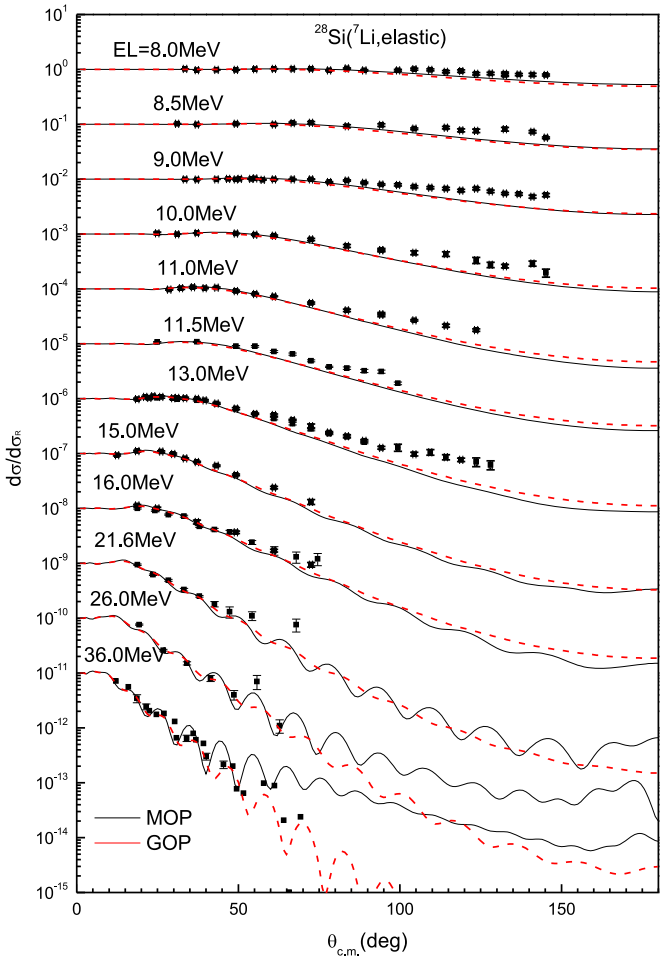

Figure 8. Calculated elastic-scattering angular distributions in the Rutherford ratio for ^{28}Si target compared with experimental data [34–36]. The solid lines and dashed lines denote the results calculated by the MOP and the GOP [11], respectively.

incident energies from 90 MeV to 200 MeV. For ^{nat}Cu, overestimation happens at incident energy 160 MeV, while the prediction above 250 MeV is in the error band of experimental data. For ^{208}Pb, the calculated results by the MOP are in reasonable agreement with experimental data below 70 MeV but give an underestimation above 300 MeV.

For ^{27}Al [55, 56], ^{64}Zn [1], ^{116}Sn [2], and ^{138}Ba [57], the experimental data are only available at incident energies below 50 MeV and the MOP reproduces the experimental data well as shown in figure 15.

It can be seen that the calculated elastic-scattering angular distributions by the MOP underestimate the experimental data at large scattering angles for some cases, especially for ^{120}Sn and ^{144}Sm. On the other hand, the calculated results become larger than the measured data on ^{40,44,48}Ca at large angles. We expect the discrepancy is caused by the breakup effect. In order to qualitatively analyze the discrepancy, the nearside/farside (N/F) decomposition of the scattering amplitude [25, 58, 59] is performed. The elastic scattering amplitude, $f(\theta)$, is decomposed into the nearside and farside component as

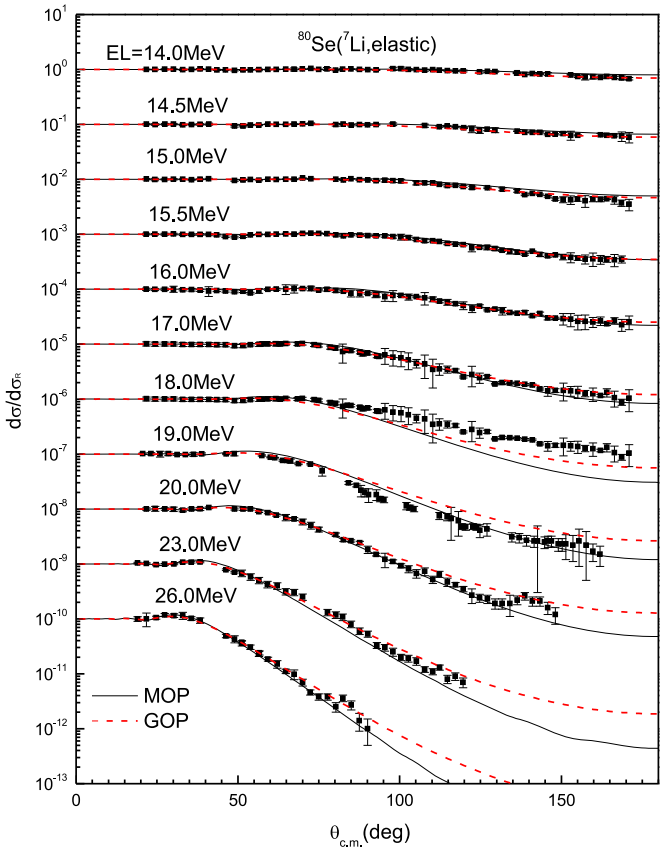

Figure 9. Same as figure 8 but for ^{80}Se. The experimental data are taken from [37].

$$f(\theta) = f_N(\theta) + f_F(\theta), \tag{10}$$

where $f_N(\theta)$ and $f_F(\theta)$ are the sum of Coulomb and nuclear part of the nearside and farside, respectively, as

$$f_N(\theta) = f_N^{(\mathrm{coul})}(\theta) + f_N^{(\mathrm{nucl})}(\theta), f_F(\theta) = f_F^{(\mathrm{coul})}(\theta) + f_F^{(\mathrm{nucl})}(\theta). \tag{11}$$

Here, $f_N^{(\mathrm{coul})}$ ($f_F^{(\mathrm{coul})}$) is the nearside (farside) component of the Coulomb amplitude, expressed with analytical form [58]. The nearside and farside component of the nuclear part, $f_N^{(\mathrm{nucl})}$ and $f_F^{(\mathrm{nucl})}$, are expressed with the element of the S-matrix, S_L, as

$$f_{N,F}^{(\mathrm{nucl})} = \frac{\mathrm{i}}{2k}\sum_L (2L+1)\mathrm{e}^{2\mathrm{i}\sigma_L}(1 - S_L)Q_L^{(\mp)}(\cos\theta), \tag{12}$$

where $Q_L^{(-)}$ and $Q_L^{(+)}$ are the traveling wave components of the Legendre polynomial [58], corresponding to the nearside and farside, respectively. σ_L is the Coulomb phase shift.

It should be noted that the N/F decomposition is suitable for non-spin condition only and the spin–orbit coupling potential is ignored when we used it, as the influence of the spin–orbit coupling potential is small. The N/F decomposition for ^{7}Li+^{40}Ca reaction at EL = 34.0 MeV and ^{7}Li+^{120}Sn at EL = 28.0 MeV are shown in figure 16. The calculated elastic-scattering angular distributions without the spin–orbit coupling potential are almost the same as the original results for ^{120}Sn and are quite alike for ^{40}Ca, which means that the N/F

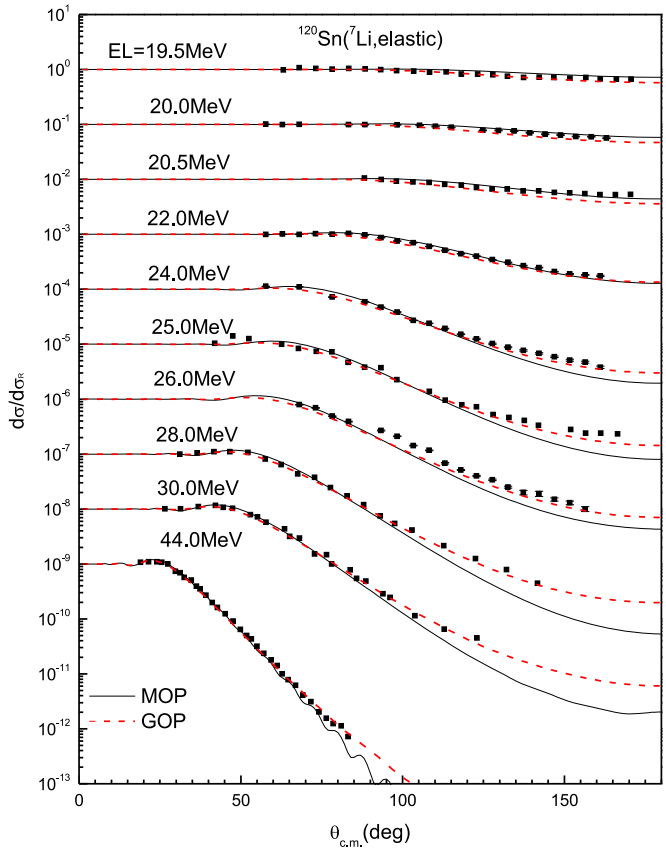

Figure 10. Same as figure 8 but for ^{120}Sn. The experimental data are taken from [38–40].

decomposition is practicable for the MOP. For ^{40}Ca target, the Fraunhofer crossover [59] between the nearside and the farside occurs around 60° and the farside dominates the scattering for angles larger than the crossover point, which causes an overestimation on the experimental data for large angles. On the contrary, the nearside dominates scattering amplitude overall for ^{120}Sn and an underestimation occurs.

Therefore, in order to get a better agreement with the experimental data, the farside for ^{40}Ca should decrease and the nearside for ^{120}Sn should increase at large angles. Both of the changes imply a reduction of the strength of the real potential and an increase of the strength of the imaginary potential [25, 59], which is regarded to be caused by the breakup effect. Therefore, the breakup coupling to the elastic channel is important in some cases and should be considered in some meticulous analyzes. The study of the breakup mechanism and the effect of the breakup coupling to the elastic channel will be our next-step work.

We also try to apply the MOP to light target nuclei, and calculate the elastic-scattering angular distributions for ^{11}B and ^{12,13}C. As shown in figure 17, the calculated results by the MOP are consistent with the tendency of experimental data [60–63, 34, 64], while the magnitude has some discrepancy. The MOP is not appropriate for these light nuclei. The reason maybe that the breakup effect of both projectile and target nuclei is not considered

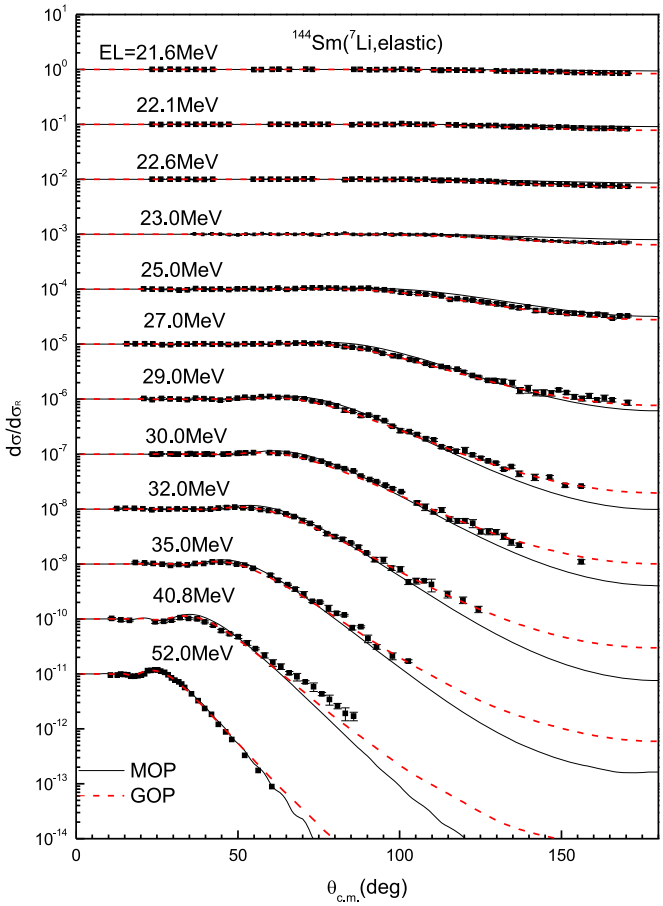

Figure 11. Same as figure 8 but for ^{144}Sm. The experimental data are taken from [33, 41].

here, and the Negele's formula [65] for obtaining the nuclear density of target nuclei used in the calculation of the nucleon MOP [12, 18–20] is not suitable for such light nuclei. In addition, it can be seen that the GOP results seriously underestimate the experimental data and are much worse than MOP results above 40°.

4. Summary and conclusions

We obtained a MOP for ^{7}Li without free parameter by folding model based on Skyrme nucleon–nucleon effective interaction. The internal wave function of ^{7}Li is obtained by the cluster model, and the ground-state energy (−2.47 MeV), the charge form factor of electron elastic scattering, and the r.m.s matter radius and charge radius are reproduced well. The elastic-scattering angular distributions and reaction cross sections for target nuclei from ^{27}Al to ^{208}Pb at incident energies up to 450 MeV are calculated by the ^{7}Li MOP. Generally, the MOP reproduces the experimental data of the reaction cross sections basically. The MOP can predict the elastic scattering angular distributions rather well for the target nuclei from ^{27}Al to

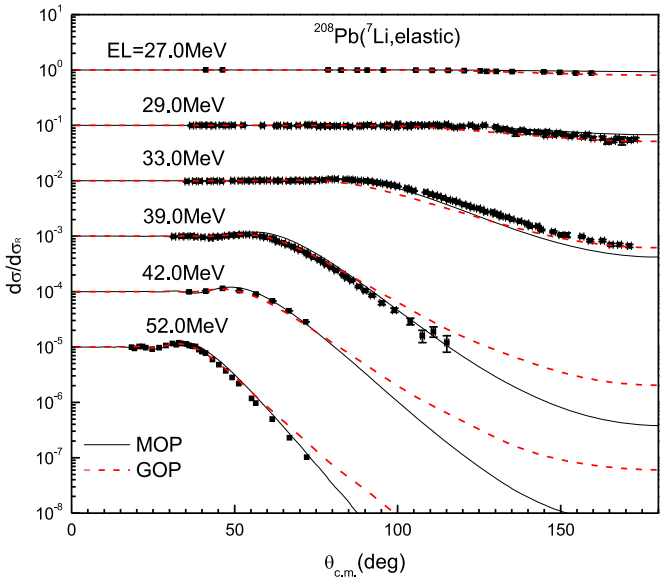

Figure 12. Same as figure 8 but for ^{208}Pb. The experimental data are taken from [6, 42–44].

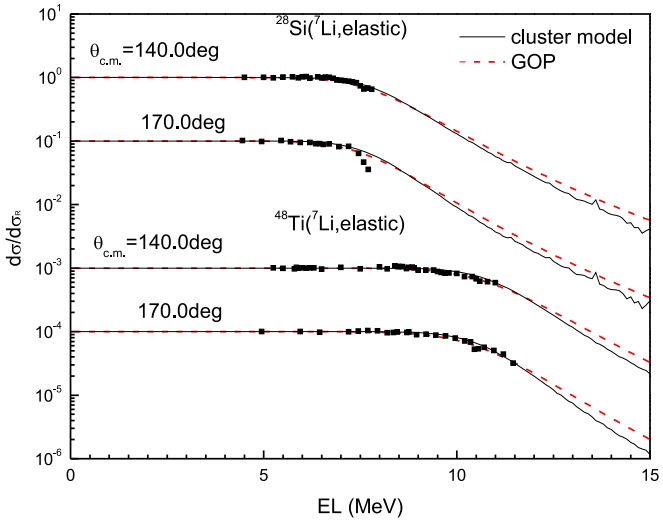

Figure 13. Calculated elastic-scattering angular distributions in the Rutherford ratio for ^{28}Si and ^{48}Ti at some scattering angles compared with experimental data [45–47]. The solid lines and dashed lines denote the results calculated by the MOP and the GOP [11], respectively.

^{208}Pb at forward angles, while at relatively large scattering angles, there are some discrepancies between the theoretical results and the experimental data in some cases, which is expected to be caused by not considering the breakup effect. The MOP is comparable to the

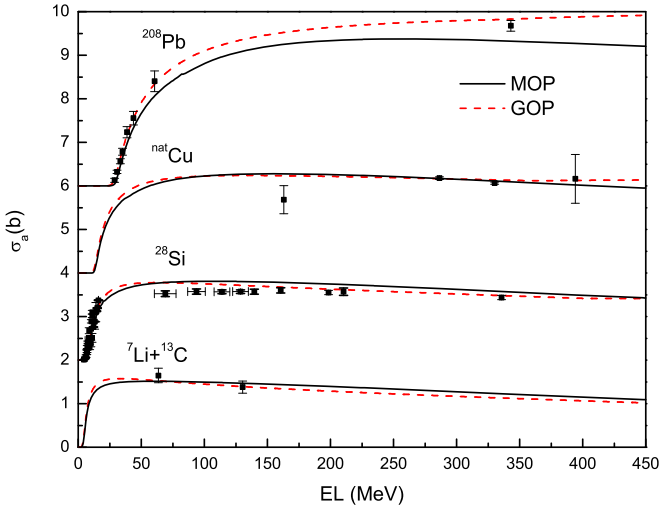

Figure 14. Reaction cross sections calculated by the MOP compared with experimental data for ^{13}C [48], ^{28}Si [49–53], ^{nat}Cu [54] and ^{208}Pb [41, 43] targets and the results calculated by the GOP [11]. The data are shifted upwards by adding 0, 2, 4 and 6 b, respectively. The solid lines and dashed lines denote the results calculated by the MOP and the GOP, respectively.

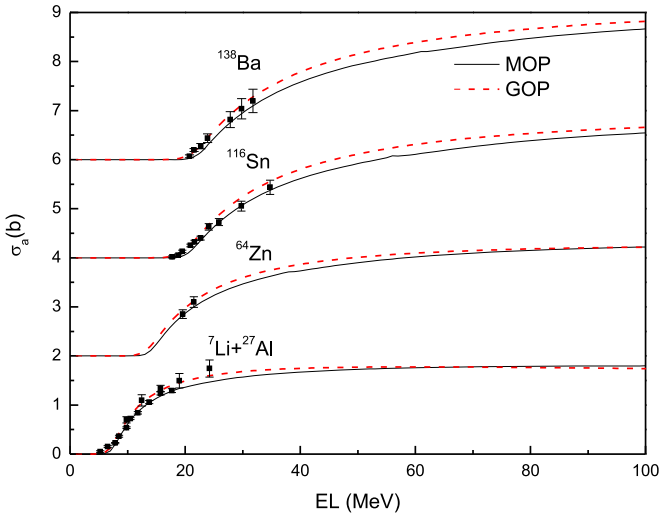

Figure 15. Same as figure 14 but for ^{27}Al, ^{64}Zn, ^{116}Sn and ^{138}Ba. The experimental data are taken from [1, 2, 55–57].

GOP in reproducing the experimental data in many cases. The quantitative investigation of the breakup effect in ^{7}Li-nucleus interaction by using CDCC will be our next-step subject. This work has prepared the $t + \alpha$ cluster description of ^{7}Li and the MOPs of triton and alpha particle for the analysis.

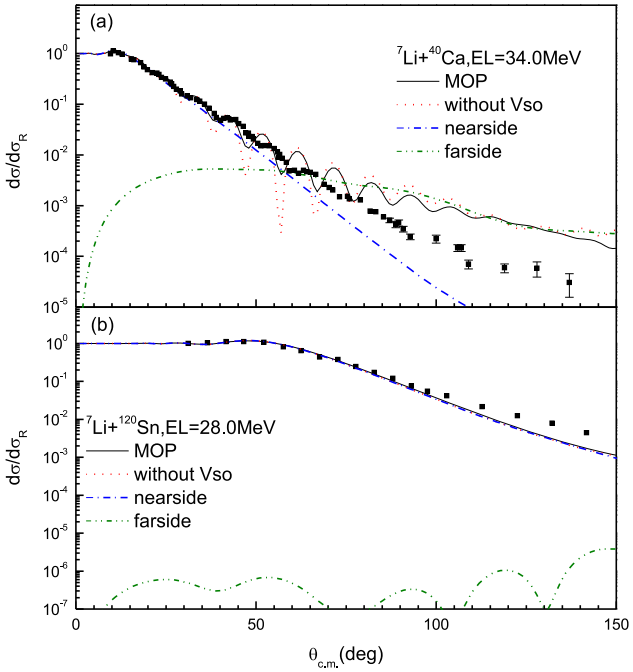

Figure 16. The nearside/farside decomposition of the elastic scattering for (a) ^{7}Li+^{40}Ca at EL = 34.0 MeV and (b) ^{7}Li+^{208}Sn at EL = 28.0 MeV. The solid lines represent the calculated elastic-scattering angular distributions by the MOP directly and the doted lines are the calculated results when the spin–orbit coupling potential is ignored. The dashed–dotted lines and the dashed–dotted–dotted lines donate the nearside and farside components without spin–orbit coupling potential, respectively.

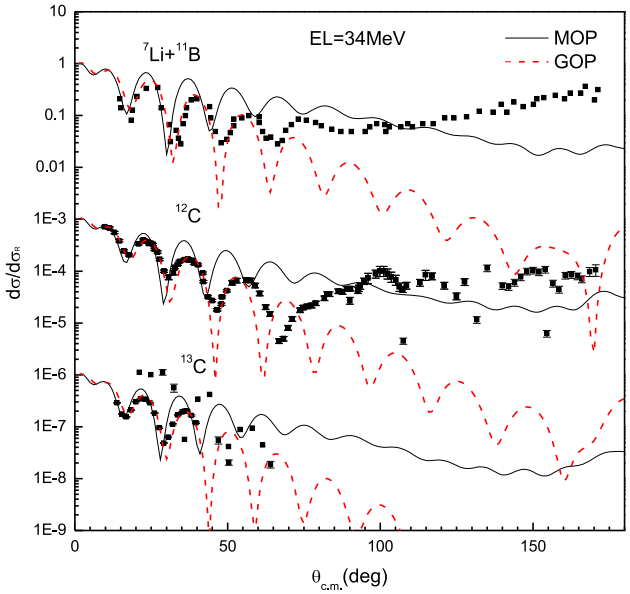

Figure 17. Same as figure 5 but for ^{11}B and ^{12,13}C. The experimental data are taken from [60–63, 34, 64].

Acknowledgments

We would like to thank Takuma Matsumoto for the helpful discussions. This work was supported by the National Natural Science Foundation of China (11705009) and Science Challenge Project (TZ2018005).

ORCID iDs

Wendi Chen https://orcid.org/0000-0002-1554-8090
Weili Sun https://orcid.org/0000-0002-0572-1339

References

[1] Gomes P R S *et al* 2005 *Phys. Rev.* C **71** 034608
[2] Deshmukh N N *et al* 2011 *Eur. Phys. J.* A **47** 118
[3] Kuterbekov K, Kabyshev A and Azhibekov A 2017 *Chin. J. Phys.* **55** 2523–39
[4] Maiti M and Lahiri S 2010 *Phys. Rev.* C **81** 024603
[5] Oulebsir N *et al* 2012 *Phys. Rev.* C **85** 035804
[6] Zeller A, Weisser D, Ophel T and Hebbard D 1979 *Nucl. Phys.* A **332** 515–24
[7] Sanderson D P, Van Verst S P, Cook J, Kemper K W and Eck J S 1985 *Phys. Rev.* C **32** 887–93
[8] Kuterbekov K A *et al* 2014 *Phys. At. Nucl.* **77** 581–6
[9] Steeden M F, Coopersmith J, Cartwright S J, Cohler M D, Clarke N M and Griffiths R J 1980 *J. Phys. G: Nucl. Phys.* **6** 501–9
[10] Glover C W, Cutler R I and Kemper K W 1980 *Nucl. Phys.* A **341** 137–48
[11] Xu Y, Han Y, Hu J, Liang H, Wu Z, Guo H and Cai C 2018 *Phys. Rev.* C **97** 014615
[12] Shen Q B, Han Y L and Guo H R 2009 *Phys. Rev.* C **80** 024604
[13] Guo H, Xu Y, Han Y and Shen Q 2010 *Phys. Rev.* C **81** 044617
[14] Guo H, Xu Y, Liang H, Han Y and Shen Q 2014 *Nucl. Phys.* A **922** 84–98
[15] Guo H, Zhang Y, Han Y and Shen Q 2009 *Phys. Rev.* C **79** 064601
[16] Guo H, Xu Y, Liang H, Han Y and Shen Q 2011 *Phys. Rev.* C **83** 064618
[17] Guo H, Liang H, Xu Y, Han Y, Shen Q, Cai C and Ye T 2017 *Phys. Rev.* C **95** 034614
[18] Xu Y, Guo H, Han Y and Shen Q 2017 *EPJ Web. Conf.* **146** 12021
[19] Xu Y, Guo H, Han Y and Shen Q 2014 *J. Phys. G: Nucl. Part. Phys.* **41** 015101
[20] Xu Y, Guo H, Han Y and Shen Q 2017 *Phys. Rev.* C **96** 024621
[21] Satchler G 1979 *Nucl. Phys.* A **329** 233–58
[22] Khoa D T and Satchler G 2000 *Nucl. Phys.* A **668** 3–41
[23] Bell J S and Squires E J 1959 *Phys. Rev. Lett.* **3** 96–7
[24] Saito S 1969 *Prog. Theor. Phys.* **41** 705–22
[25] Sakuragi Y, Yahiro M and Kamimura M 1986 *Prog. Theor. Phys. Suppl.* **89** 136–211
[26] Horiuchi H 1977 *Prog. Theor. Phys. Suppl.* **62** 90–190
[27] Buck B, Friedrich H and Wheatley C 1977 *Nucl. Phys.* A **275** 246–68
[28] Suelzle L R, Yearian M R and Crannell H 1968 *Phys. Rev.* **168** 1414–1414
[29] Tanihata I, Hamagaki H, Hashimoto O, Shida Y, Yoshikawa N, Sugimoto K, Yamakawa O, Kobayashi T and Takahashi N 1985 *Phys. Rev. Lett.* **55** 2676–9
[30] Cutler R I, Nadworny M J and Kemper K W 1977 *Phys. Rev.* C **15** 1318–24
[31] Morrison T P, Jones G D, Ekstrom L P, Kearns F, Lornie P R G, Mustaffa O, Price H G, Simister D N, Twin P J and Wadsworth R 1979 *J. Phys. G: Nucl. Phys.* **5** 1751–60
[32] Clark P, Ophel T, Eck J, Zeller A, Nurzynski J, Weisser D and Hebbard D 1980 *Nucl. Phys.* A **349** 258–70
[33] Clark P, Ophel T, Nurzynski J, Atwood C and Hebbard D 1981 *Nucl. Phys.* A **352** 267–78
[34] Schumacher P, Ueta N, Duhm H, Kubo K I and Klages W 1973 *Nucl. Phys.* A **212** 573–99
[35] Pakou A *et al* 2004 *Phys. Rev.* C **69** 054602
[36] Sinha M, Roy S, Basu P, Majumdar H, Santra S, Parkar V, Golda K and Kailas S 2011 *EPJ Web Conf.* **17** 03004

[37] Furumoto T, Horiuchi W, Takashina M, Yamamoto Y and Sakuragi Y 2012 *Phys. Rev.* C **85** 044607
[38] Sousa D *et al* 2010 *Nucl. Phys.* A **836** 1–10
[39] Zagatto V A B *et al* 2017 *Phys. Rev.* C **95** 064614
[40] Kundu A, Santra S, Pal A, Chattopadhyay D, Tripathi R, Roy B J, Nag T N, Nayak B K, Saxena A and Kailas S 2017 *Phys. Rev.* C **95** 034615
[41] Figueira J M *et al* 2010 *Phys. Rev.* C **81** 024613
[42] Parkar V V, Jha V, Roy B J, Santra S, Ramachandran K, Shrivastava A, Chatterjee A, Jain S R, Jain A K and Kailas S 2008 *Phys. Rev.* C **78** 021601
[43] Keeley N, Bennett S, Clarke N, Fulton B, Tungate G, Drumm P, Nagarajan M and Lilley J 1994 *Nucl. Phys.* A **571** 326–36
[44] Gupta D, Samanta C, Chatterjee A, Kailas S, Roy B, Mahata K and Shrivastava A 2001 *Nucl. Phys.* A **683** 3–20
[45] Räisänen J and Rauhala E 1993 *Nucl. Instrum. Methods Phys. Res.* B **73** 439–42
[46] Rauhala E and Räisänen J 1994 *J. Appl. Phys.* **75** 642–4
[47] Nurmela A, Rauhala E and Räisänen J 1999 *Nucl. Instrum. Methods Phys. Res.* B **155** 211–20
[48] Carstoiu F, Trache L, Tribble R E and Gagliardi C A 2004 *Phys. Rev.* C **70** 054610
[49] Warner R E *et al* 1996 *Phys. Rev.* C **54** 1700–9
[50] Sobolev Y *et al* 2005 *Bull. Russ. Acad. Sci.: Phys.* **69** 1790–5
[51] Pakou A *et al* 2007 *Phys. Rev.* C **76** 054601
[52] Pakou A *et al* 2009 *Eur. Phys. J.* A **39** 187–94
[53] Musumarra A *et al* 2010 *Nucl. Instrum. Methods Phys. Res.* A **612** 399–406
[54] Saint-Laurent M G *et al* 1989 *Z. Physik* A **332** 457–65
[55] Kalita K *et al* 2006 *Phys. Rev.* C **73** 024609
[56] Benjamim E *et al* 2007 *Phys. Lett.* B **647** 30–5
[57] Maciel A M M *et al* 1999 *Phys. Rev.* C **59** 2103–7
[58] Fuller R C 1975 *Phys. Rev.* C **12** 1561–74
[59] McVoy K and Satchler G 1984 *Nucl. Phys.* A **417** 157–73
[60] Cook J, Stephens M and Kemper K 1987 *Nucl. Phys.* A **466** 168–88
[61] Cook J, Abdallah A K, Stephens M N and Kemper K W 1987 *Phys. Rev.* C **35** 126–36
[62] Vineyard M F, Cook J, Kemper K W and Stephens M N 1984 *Phys. Rev.* C **30** 916–24
[63] Bartosz E E, Keeley N, Cathers P D, Cooper M W, Kemper K W, Maréchal F and Rusek K 2001 *Phys. Rev.* C **64** 014606
[64] Li Y J *et al* 2012 *Eur. Phys. J.* A **48** 13
[65] Negele J W 1970 *Phys. Rev.* C **1** 1260–321